Dislocation structures in nanoindented ductile metalsa transmission electron microscopy direct observation

S Graça, P A Carvalho, R Colaço

Dislocation structures in nanoindented ductile metals – a TEM direct observation

S. Graça[1], P. A. Carvalho[2], R. Colaço[3]*

[1]EMPA Materials Science and Technology, Feuerwerkerstrasse 39, CH-3602 Thun, Switzerland

[2]Department of Bioengineering and ICEMS, Instituto Superior Técnico, TU Lisbon, Av. Rovisco Pais, 1049-001 Lisboa, Portugal

[3]Department of Bioengineering and CQE, Instituto Superior Técnico, TU Lisbon, Av. Rovisco Pais, 1049-001 Lisboa, Portugal

* Corresponding author. Tel./fax: +351 218418120.

E-mail address: rogerio.colaco@ist.utl.pt (R. Colaço).

PACS: 68.37.Lp, 61.72.Ff, 62.20.Qp

Abstract

Several attempts have been made over recent years to understand Indentation Size Effect (ISE). The theoretical models, based essentially on strain gradient plasticity theories, such as the Nix-Gao model, predicts that ISE is caused by an increase of the density of dislocations as the indentation size decreases. MD simulation results tend to confirm this fact, but the truth is that very few experimental studies exists on the direct observation of how dislocations are generated and accommodated in the vicinity of nanoindentations. In this study, by using a Ni TEM thin foil as model material, we show that when the material is submitted to AFM-based nanoindentations a high dislocation density zone is generated at the centre of the indented region, and that prismatic loop and helical dislocations are emitted sidewards from the central region of the nanoindentation along the $\langle 110 \rangle$ directions. Moreover, we show that the dislocation array formed during the nanoindentation process is far from the ideal model proposed by Nix and Gao, based on load axi-centered dislocation loops. With this study we aim at contributing to a better comprehension of ISE mechanisms in ductile metals.

Keywords: Nanondentation ; dislocations; AFM; TEM; Nickel.

1. Introduction

The contact between nominally flat surfaces, in dry or boundary lubrication conditions, frequent in rubbing engineering components, occurs between surface asperities whose contact areas can be of only a few tens of square nanometres or even smaller [1]. At this scale of contact the plastic response of a material may differ significantly from that at the micro and macro scales. In fact, it has been shown that hardness greatly increases with decreasing indentation depth in the submicrometric depth range (see, for instance, [2-10]). This effect is commonly known in the literature as indentation size effect (ISE). Since the wear resistance of a wide range of materials, in particular metals and metallic alloys, is closely related with its hardness [11-13], understanding the origins of ISE and its impact on wear behaviour is fundamental to optimize the tribo-performance of materials.

One of the factors that greatly affects the resistance of a material to plastic deformation when the scale decreases is the presence of large strain gradients [14]. In the particular case of indentation, geometrically necessary dislocations (GNDs) must be created to accommodate the plastic strain gradients surrounding the indentation. In general, the magnitude of these gradients is inversely proportional to the length scale over which the deformation occurs [14]. Therefore, as the size of the indentation decreases, the density of GNDs increases. Some models, such as the well-know Nix-Gao model [15] and extensions of this model [8, 10, 16-21], have been developed in order to understand this relation between the deformation scale dependence of dislocation density and the ISE exhibited by many materials. However, the assumptions of these models are simple regarding the crystallographic nature of materials and a lack of fundamental understanding of the true origins of ISE still exists. This challenging

objective can only be achieved with the help of powerful experimental techniques, and no doubt that the direct visualization of indented regions by transmission electron microscopy (TEM) is one of the most important ones due to the small scale information that it can supply. Nevertheless, the use of this technique to understand the fundamentals of ISE is scarce [22-25] and more studies in a wide range of materials are still needed.

Although the experimental set-up for performing in situ TEM nanoindentations is currently available (e.g. [26]), we have used a different approach. In this work nanoindentations were performed in electron transparent regions of Ni TEM samples by using an AFM diamond tip, and the dislocation structures produced at the nanometric contact scale were subsequently observed by TEM. Contrarily to other experimental and theoretical indentation studies, where the direction of load application is usually parallel to a specific low-index zone axis, in the present work the indenter was arbitrarily oriented. This less constrained approach enabled to evaluate the nanoscale plastic response of the material under generic crystallographic orientation conditions and allowed to frame the results found in the literature for low-index zone axis indentation.

Nickel was chosen as model material for this study for several reasons: a) it is the main constituent of one of the most frequently used families of hardfacing alloys [27]; b) it is well understood from the microstructural point of view (presents an FCC structure, relatively high stacking fault energy and no phase transformations), which simplifies the analysis of the deformation mechanisms; c) this material exhibits a strong ISE [10, 28], and, moreover that ISE can be fitted by the Nix-Gao model in a consistent manner [29].

2. Experimental methods

A nickel polycrystalline coating, about 1 mm thick, was deposited on an AISI 304 stainless steel substrate by powder injection laser cladding using a 3 kW CO_2 fast axial flow laser with a transverse electromagnetic 01* mode. The clad parameters and microstructural characterisation were described in a previous paper by the authors [10].

The thick nickel coating was cut from the substrate with a thin low speed abrasive saw and ground with SiC abrasive papers down to a foil thickness of ~ 60 μm. 3 mm discs were cut from this thin foil with a 70 W Q-switched Nd/YAG laser and ion milled to perforation using a 4 kV Ar^+ beam and a 12º incidence angle. After ion milling, electron transparent regions were present in the periphery of the hole created at the centre of the discs.The thickness of Ni TEM samples prepared in the same way as those of this work has been estimated in a previous work [29] and is in the range of 100 to 200 nm.

Arrays of nanoindentations with a spacing of about 1 μm were generated in electron transparent regions of the TEM samples using a Veeco DNISP atomic force microscopy (AFM) probe mounted in a Veeco CP-II instrument. This probe type consists of a 3-sided pyramidal diamond tip, with tip apex angle of ~ 95º and curvature radius smaller than 50 nm, mounted on a stainless steel cantilever with normal spring constant of 215.8 N/m (Figure 1). The applied load was approximately 50 μN. Details of the procedure can be found in [10].

The regions containing nanoindentations were observed by AFM by means of the same equipment previously described using commercial silicon probes in contact mode, and by TEM with a Hitachi H-8100 transmission electron microscope operated at

200 kV. The software Carine Crystallography 3.1 (distributed by Divergent S. A.) was used to simulate diffraction patterns and stereographic projections.

3. Results

Figure 2.a shows an AFM image in contact mode of the TEM thin foil in the transparent region near the edge of the inner central hole (upper right corner in the figure). Indicated by the arrow, one of the nanoindentations can be clearly observed. In figure 2.b it is shown the topographical profile across this nanoindentation. It can be observed that, from the upper part of the small lateral pile-up, formed at the edge of the indentation, to the bottom of the indentation the height is scarcely smaller than 10 nm. This fact means that the indentations are less than 1/10 of the thickness of the TEM thin foil. Therefore, we will assume, as a reasonable approach to the interpretation of the results, that the effect of the small thickness of the sample in the dislocation structure can be neglected. Moreover, it should be noted that the thickness of the thin foil is much larger than the thickness considered in the MD simulations, e.g, in Al (no more than a few tens of nanometers) [30-32].

Figure 3.a and b show Bright-Field (BF) TEM images of a dendrite, respectively, before and after nanoindentation with the DNISP probe. By comparing images 3.a and b, it is possible to observe that the two straight dislocations pointed in figure 3.c were not present before the test. Indeed, the indentations that were performed closer to the few dislocations which might previously be present in the grain, and may interfere in the dislocation propagation paths, were not considered in the analysis. The white arrows in Figure 3.b point to nanoindentation rows. It is worth mentioning that the study of the interaction of the indentation-generated dislocations with grain boundaries is beyond the

purpose of this work and therefore, only the indentations in the inner part of the grain were analyzed. The magnified detail of an indented region in Figure 3.c shows that the dislocation structure created is formed by a high dislocation density zone at the central region (F), from where pileups of helical prismatic dislocations (H) and prismatic dislocation loops (L) as well as nearly straight dislocation lines (S) are emitted. The typical triangular shape of indentations made by 3-sided pyramidal indenters cannot be identified by the contour or within the high dislocation density zone, therefore a white triangle with the approximate shape and size of the indentations was introduced in Figure 3.c. Tilting experiments demonstrated that the consistently dark contrast observed in the indentation regions did not result from thickness variations. The elastic fields associated with the dislocations cause both density and crystallographic orientation changes and this is compatible with the presence of dislocation forests, i.e. a very high dislocation density zone in this region.

As can be observed from Figure 3.c, the loops and helices with diameters of a few tens of nanometres are piled-up along typically 3 specific crystallographic directions emanating from the indentation centres, suggesting that loop and helical dislocations are punch-out due to the high compressive stress state due to the indentation, similarly to the observations of Steinman *et al.* in Si crystals [33]. The spacing between successive loops and helix turns is comparable to the loops/helices diameters. Since Ni has an FCC structure, the loops and helices emitted from the indented regions are expected to glide (and pile up) along $\langle 110 \rangle$ directions and are composed of segments lying on two linearly independent slip systems (Figure 5.a). Electron diffraction patterns obtained with the electron beam close to the $[011]$ direction were used to establish the orientation

of the $[011]$ stereographic projection and identify the loops/helices gliding direction projections (see Figure 4).

In addition, piled up dislocations were characterized by conventional TEM experiments using the $g \cdot b = 0$ invisibility criterion, where g is the reciprocal lattice vector for the *hkl* reflection [34]. Selected area diffraction (SAD) patterns, taken along $[010]$ and $[011]$ zone-axes and consistently indexed, were used as starting points to obtain the two-beam conditions used for the visualization of the dislocation structures. Figure 5 shows BF TEM images of indented regions, taken under three different two-beam conditions: $g = 200$ ((a) with a magnified detail in (b)); $g = 00\bar{2}$ ((c) with a magnified detail in (d)); $g = \bar{1}\,\bar{1}\,1$ ((e) with a magnified detail in (f)). In general two invisibility conditions are required to determine Burgers vectors, however, the high stacking fault energy of nickel [35] and the absence of stacking fault contrast in the images allowed to assume that the dislocations present were perfect and the Burgers vectors of the pileup structures could be unequivocally indentified by the selected two-beam conditions (see Table 1). Pileups along direction *a* are visible in Figure 5.a, b and e, f but are invisible in c, d, which implies $b = \pm\frac{1}{2}[110]$, whereas the loops along direction *b* can be observed in Figure 5 .a,b, c,d and e,f, which implies $b = \pm\frac{1}{2}[\bar{1}01]$. On the other hand, pileups along *c* are visible with g = 200 (Figure 5.a) and invisible with the other conditions implying $b = \pm\frac{1}{2}[\bar{1}10]$ (we note that the *a*, *b* and *c* directions are crystallographic directions along which the emitted loops piled up. As such, the projections of those directions on Figure 5 change with the tilting angles imposed on the crystal to obtain visibility and invisibility two-beam diffraction conditions). A faint residual contrast was detected for loops/helices along *a* in Figure 5.d, which is attributed to partial satisfaction of the invisibility condition for edge dislocations ($g \cdot b = 0$ and

$g \cdot b \times u = 0$, where u is a unit vector along the dislocation line) [34]. The weaker contrast of the central region of the high dislocation density zone for $g = \bar{1}\,\bar{1}\,1$ is not in agreement with a balanced presence of dislocations with these three types of Burgers vectors but would be compatible with an additional presence of dislocations with b $=\pm\frac{1}{2}[101]$ (see Figure 4.b and Table 1). These results are therefore in agreement with the projected $\langle 110 \rangle$ directions in Figure 4.b. Lower magnification images showed that this behaviour was general for the indentation arrays.

The direction of load application was parallel to the electron beam for the untilted sample. Tilting experiments to and from the $[011]$ diffraction pattern enabled to establish the direction of load application as $\sim[\bar{1}\,54]$ (marked with a star in the stereographic projection of Figure 4.b). The resolved shear stress associated with each $\langle 110 \rangle$ direction was assessed assuming, on a first approximation, an uniaxial state of stress (Table 2). The results show that, for the current crystallographic configuration, similar high resolved shear stresses occur in one of the slip systems associated with the $\pm\frac{1}{2}[110]$, $\pm\frac{1}{2}[\bar{1}01]$ and $\pm\frac{1}{2}[\bar{1}10]$ Burgers vectors, which agree with the specific $\langle 110 \rangle$ pileup directions determined with the TEM observations.

4. Discussion

4.1) Indented regions observed by TEM

TEM observations of the nanoindented regions showed that at the nanometric contact scale the plastic deformation is accommodated through three mechanisms: 1) formation of a high dislocation density region in the neighbourhood of the indentation; 2) emission of prismatic loops and helix dislocations from the centre of the indented

region that tended to pile up along ~500 nm; 3) in a few cases, emission of straight dislocations.

In this way, two distinct regions are formed: a) a high dislocation density region in the inner vicinity of the indentation, resulting from mechanism 1; b) a low dislocation density region surrounding the previous one, resulting from mechanisms 2 and 3. The high dislocation density at the inner region suggests dislocation locking, which can occur through formation of non-conservative jogs due to the intersection of screw dislocations, or other mechanisms, such as Lomer-Cottrell locks, common in FCC materials [36]. Since locked dislocations cannot glide as the indenter is further pressed against the sample, plastic deformation may proceed through the formation and gliding of helical/loop dislocations (mechanism 2) and, less frequently, with the formation of straight dislocations (mechanism 3). Indeed, the fact that parallel pileups were not observed along the indentation depth indicates that loops/helices emission occurred only at the highest stress level towards the end of each indentation test and not continuously during load application.

Recent TEM observations of nanoindentations in a Cu single crystal [22], a Ni3Al(Cr,B) single crystal [23], Ni3Al [25], and Ti-6Al-4V [24] showed also an accumulation of dislocations in the neighbourhood of the indented region and emission of dislocations from this high dislocation density region.

Molecular dynamics (MD) simulations of nanoindentation experiments on an Al (111) single crystal with a spherical indenter [30-32] showed that plasticity begins with the homogenous nucleation of a few dislocation loops (designated as glide loops by Li *et al.* [30]), which then expand and intersect each other, producing sessile dislocation segments. As the indenter is further displaced, prismatic dislocation loops with the

shape of a rhombus are emitted from this region and glide along <110> directions, as shown schematically inFigure 6. Due to the high strain energy associated with the corners of the rhombus, some bending of the dislocation line may occur, especially at the sharpest corners of 70.53º if the dislocation energy is fairly independent of the crystallographic direction as in Ni.

The repeated pattern of loops/helices propagation (Figure 4) show that these defect structures glided only along directions associated with the three slip systems of highest resolved shear stress (Table 2). Therefore, although one could expect that the indenter geometry and surface asperities may have some influence on the propagation of the dislocations, it is clear that the crystallography factor is dominant, as could be proved by the Schmid factor calculations shown in Table 2. In fact, no helical dislocations or dislocation loop pile-ups are emitted along the direction parallel to the top side facet of the triangles in Fig. 3.c and 4, which supports the dominant effect of crystallography. Therefore, these results enable thus to infer that: (i) indenter geometry and local surface asperities play a minor role in the loops/helices pileup configuration; (ii) in each loop, the segment(s) corresponding to the high resolved shear stress tends to drag the segment(s) of low/null resolved shear stress (see Figure 6 and Table 2), (iii) the resolved shear stress difference in the two linearly independent segments of each rhombus (see Figure 5.a and Table 2) can contribute for the development of helices; and, furthermore, (iv) since the difference between the resolved shear stress for the different slip systems determined assuming an uniaxial stress state is well correlated with the long range propagation (up to 500 nm) and pileup of the loop/helix structures, this behaviour seems to be strongly dependent of the (compressive) stress state

component normal to the surface. To the authors' best knowledge, this type of observation has never been reported.

A final aspect that is important to discuss is the influence of the triangular shape of the indenter on the structure of dislocations. It is clear that the non-axisymmetric shape of the indenter will create a non-uniform stress distribution around the indented region. However, as can be observed in the TEM images of the nanoindented regions (Figure 3.c and Figure 4), the angles between the projected gliding directions of the loop/helical dislocations do not match with the angles between the projected directions of the indenter edges that come together at the tip (inlet in Figure 1), thus showing that the main contribution to dislocation gliding is the material crystallography and not the indenter shape.

4.2) Correlation of results with Indentation Size Effect

Indentation experiments performed previously in laser clad Ni showed that this material exhibits a strong indentation size effect [10, 29], especially in the submicrometric depth range. Moreover, the good correlation found between the theoretical predictions of the Nix-Gao model and the hardness results indicates that the observed ISE is closely related to the increase of the density of geometrical necessary dislocations with the decrease of deformation scale [10, 28, 29], which is confirmed by the present work. In fact, the observation of high dislocation density zone at the centre of the nanoindented regions in Ni (Figure 3.c) indicates that a strong repulsion between dislocations should take place in small nanoindentations, thus increasing the resistance of the material to plastic deformation. However, the size of the high dislocation density zone (Figure 3.c) is clearly larger than the size of the indenter contact region, which is

assumed in the Nix-Gao model as the plastic zone in a conical indentation (Figure 7). Some authors have previously observed that the Nix-Gao model overestimates the hardness for small indentation depths (e.g. below 1 μm in iridium [17] and below 200 nm in MgO [18]). According to the model, the hardness increases indefinitely when $h \rightarrow 0$, as a result of the increase of the density of GNDs. Swadener *et al*. [17] suggested that, for very small depths, the strong repulsive forces between GNDs would cause them to spread beyond the hemispherical volume defined by the contact radius "a" (Figure 7), resulting in a density of GNDs smaller than that assumed in the Nix-Gao model. In fact, a few years later, Feng and Nix [18] and Durst et al. [19, 35] showed that the overestimation of the density of GNDs in the Nix-Gao model can be compensated by assuming an effective radius of the plastic zone $f.a$ larger than a, where $1 < f < 2.4$ for several metallic materials, which results in an increase of the storage volume for GNDs.

This work confirms experimentally previous works by Swadener *et al*. [17], Feng and Nix [18] and Durst et al. [19, 37] since it is clearly shown that the high dislocation density zones in the indented regions in Ni are substantially larger than the indentation region. In addition to the dislocations in the high dislocation density zone, the pileups of dislocation loops/helices around this zone (Figure 3.c, Figure 4 and Figure 5.b) may also contribute to the ISE.

In order to analyse the magnitude of this contribution, an estimation of the backforce caused by these piled-up structures has been performed. As first approximation, the self-energy of a circular dislocation loop, W_S, can be performed [35]:

$$W_S = \frac{Gb^2 r}{2(1-\nu)}\left(\ln\frac{8r}{z_0} - 1\right), \qquad (1)$$

where r is the radius of the loops, z_0 the separation distance between successive loops, b the Burgers vector, G the shear modulus and ν the Poisson's ratio. The derivative of Eq. 1, yields the corresponding force associated to a loop, F_S:

$$F_S = \frac{dW_S}{dz_0} = -\frac{Gb^2 r}{2(1-\nu)z_0}. \quad (2)$$

The total force associated to the three loop pileups around an indentation, $[F_S]_{total}$, can then be calculated from:

$$[Fs]_{total} = 3nF_S = 3\left(\frac{L}{z_0}+1\right)F_s, \quad (3)$$

where n is the number of loops in a pileup and L is the length of the pileup. By combining Eqs. 2 and 3, the absolute value of $[F_S]_{total}$ is given by:

$$[Fs]_{total} = 3\left(\frac{L}{z_0}+1\right)\frac{Gb^2 r}{2(1-\nu)z_0}. \quad (4)$$

From the TEM images in Figure 3.c, Figure 4.a and Figure 5, it can be observed that z_0 ~ 20-80 nm and $2r$ ~ 20-50 nm, which results in average values of z_0 and r of 50 and 17.5 nm, respectively. By introducing these average values in Eq. 4, together with L ~ 500 nm and b = 0.25 nm, G = 76 GPa and ν = 0.31 for Ni [38], the resulting $[F_S]_{total}$ is about 40 nN, which is three orders of magnitude smaller than the normal load applied by the indenter (approximately 50 μN). Therefore, the major contribution to the ISE arises from the high dislocation density zone of sessile dislocations and not from the loop/helix pileups.

5. Conclusions

TEM observations of nanoindentations performed along an arbitrary [uvw] crystallographic direction in Ni crystals showed that the dislocation structure created

consists of a high dislocation density zone at the centre of the indented region, from where prismatic loop/helical dislocations, and less frequently, straight dislocations, are emitted along the more compact directions and piled up. Although the dislocation structure observed in the present work is substantially different in size and shape from the ideal Nix-Gao geometrical model, these observations, together with theoretical estimations of the force associated with the pileup dislocation structures support the fundamental idea of the Nix-Gao model, i.e. that the ISE is caused by an increase of dislocation density with decreasing indentation size.

Acknowledgements

The authors would like to thank Fundação para a Ciência e a Tecnologia (FCT) for the financial support of this research (Projects PTDC/CTM/68142/2006 and Eurocore FANAS/001 Nanoparma).

References

[1] Colaço R. Surface damage mechanisms: from nano and microcontacts to wear of materials. In: Gnecco E, Meyer E, editors. Fundamentals of Friction and Wear on the Nanoscale, Berlin: Springer-Verlag, 2007 p.453.

[2] Li H, Bradt RC. J Mater Sci 1993;28:917.

[3] Stelmashenko NA, Walls MG, Brown LM, Milman YV. Acta Metall Mater 1993;41:2855.

[4] Ma Q, Clarke DR. J Mater Res 1995;10:853.

[5] McElhaney KW, Vlassak JJ, Nix WD. J Mater Res 1998;13:1300.

[6] Liu Y, Ngan AHW. Scripta Mater 2001;44:237.

[7] Elmustafa AA, Stone DS. Acta Mater 2002;50:3641.

[8] Swadener JG, Misra A, Hoagland RG, Nastasi M. Scripta Mater 2002;47:343.

[9] Bull SJ. Z Metallkd 2003;94:787.

[10] Graça S, Colaço R, Vilar R. Surf Coat Technol 2007;202:538.

[11] Archard JF. J Appl Phys 1953;24:981.

[12] Rabinowicz E. Friction and Wear of Materials, 1st edition, New York: John Wiley and Sons; 1965.

[13] Hutchings IM. Tribology, Friction and Wear of Engineering Materials, London: Edward Arnold; 1992.

[14] Fleck NA, Muller GM, Ashby MF, Hutchinson JW. Acta Metall Mater 1994;42:475.

[15] Nix WD, Gao H. J Mech Phys Solids 1998;46:411.

[16] Qiu X, Huang Y, Nix WD, Hwang KC, Gao H. Acta Mater 2001;49:3949.

[17] Swadener JG, George EP, Pharr GM. J Mech Phys Solids 2002;50:681.

[18] Feng G, Nix WD. Scripta Mater 2004;51:599.

[19] Durst K, Backes B, Göken M. Scripta Mater 2005;52:1093.

[20] Huang Y, Zhang F, Hwang KC, Nix WD, Pharr GM, Feng G. J Mech Phys Solids 2006;54:1668.

[21] Huang Y, Feng X, Pharr GM, Hwang KC. Modelling Simul Mater Sci Eng 2007;15:S255.

[22] Fivel MC, Robertson CF, Canova GR, Boulanger L. Acta Mater 1998;46:6183.

[23] Chiu YL, Ngan AHW. Acta Mater 2002;50:2677.

[24] Viswanathan GB, Lee E, Maher DM, Banerjee S, Fraser HL. Mat Sci Eng A 2005;400:463.

[25] Wo PC, Ngan AHW, Chiu YL. Scripta Mater 2006;55:557.

[26] Lockwood AJ, Inkson BJ. J. Phys. D: Appl. Phys. 2008; 42: 035410.

[27] Crook P, Farmer HN. Friction and Wear of Hardfacing Alloys. In: Henry SD, editors. ASM Handbook - Friction, Lubrication and Wear Technology, vol. 18. Metals Park (OH): ASM International, 1992. p.758.

[28] Ma ZS, Long SG, Pan Y, Zhou Y. J. App. Phys. 2008; 103**(**4): 043512.

[29] Graça S, Colaço R, Carvalho P, Vilar R. Mat. Letters 2008; 62: 3812.

[30] Li J, Van Vliet KJ, Zhu T, Yip S, Suresh S. Nature 2002;418:307.

[31] Vliet KJV, Li J, Zhu T, Yip S, Suresh S. Phys Rev B 2003;67:104105.

[32] Lee Y, Park JY, Kim SY, Jun S, Im S. Mechanics of Materials 2005;37:1035.

[33] Steinman E.A., Tereshchenko A.N., Vdovin V.I., Misiuk A.Solid State Phenomena 2005; 108-109: 773.

[34] Edington JW. Interpretation of Transmission Electron Micrographs (Monographs in Practical Electron Microscopy in Materials Science), vol. 3. London: Macmillan; 1975.

[35] Chaudhuri D, Xie D, Lakshmanan AN. Wear 1997; 209:140.

[36] Hirth JP, Lother J. Theory of Dislocations, 2nd edition, Florida: Krieger Publishing Company; 1982.

[37] Durst K, Backes B, Franke O, Göken M. Acta Mater 2006; 54: 2547.

[38] ASM. Metals Handbook - Properties and Selection: Nonferrous Alloys and Special-Purpose Materials, 10th Edition, Vol. 2. Metals Park (OH): ASM International; 1990.

Tables

Table 1. Values of *g.b* for perfect dislocations in FCC crystals for the three reflections used to obtain the images in Figure 4. Dislocations become invisible when $g \cdot b = 0$ [28].

g / **b**	200	$00\bar{2}$	$\bar{1}\,\bar{1}\,1$
$\pm\frac{1}{2}[110]$	±1	0	±1
$\pm\frac{1}{2}[\bar{1}01]$	±1	±1	±1
$\pm\frac{1}{2}[\bar{1}10]$	±1	0	0
$\pm\frac{1}{2}[101]$	±1	±1	0
$\pm\frac{1}{2}[011]$	0	±1	0
$\pm\frac{1}{2}[01\bar{1}]$	0	±1	±1

Table 2. Schimd Factor (SF) for each of the two independent slips systems associated with perfect dislocations in FCC crystals [28]. The direction of uniaxial load application is $[\bar{1}54]$.

$b \pm\frac{1}{2}[110]$		$b = \pm\frac{1}{2}[\bar{1}01]$		$b = \pm\frac{1}{2}[\bar{1}10]$		$b = \pm\frac{1}{2}[101]$		$b = \pm\frac{1}{2}[011]$		$b = \pm\frac{1}{2}[01\bar{1}]$	
(*hkl*)	**SF**	**(*hkl*)**	**SF**	**(*hkl*)**	**SF**	**(*hkl*)**	**SF**	**(*hkl*)**	**SF**	**(*hkl*)**	**SF**
$(1\,\bar{1}\,1)$	0.078	$(\bar{1}\,\bar{1}\,\bar{1})$	0.389	$(\bar{1}\,\bar{1}\,1)$	0	$(1\,\bar{1}\,\bar{1})$	0.292	$(\bar{1}\,\bar{1}\,1)$	0	$(\bar{1}\,11)$	0.097
$(\bar{1}\,11)$	0.389	$(1\,\bar{1}\,1)$	0.097	(111)	0.467	$(\bar{1}\,\bar{1}\,1)$	0	$(\bar{1}\,1\,\bar{1})$	0.175	$(\bar{1}\,\bar{1}\,\bar{1})$	0.078

Figures

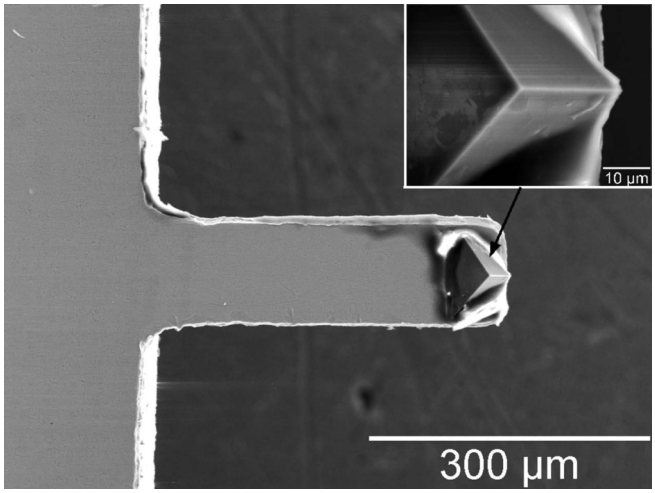

Figure 1. SEM image of AFM tip used to perform nanoindentations in Ni TEM samples. A magnified view of the triangular pyramid is shown in the inset at the top right corner of the image.

a)

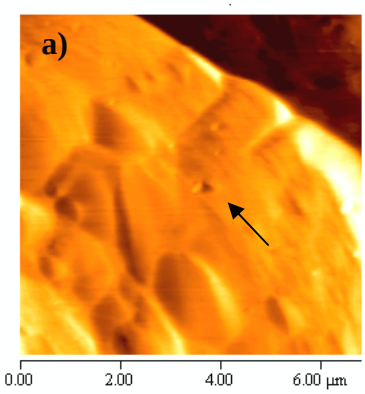

b)

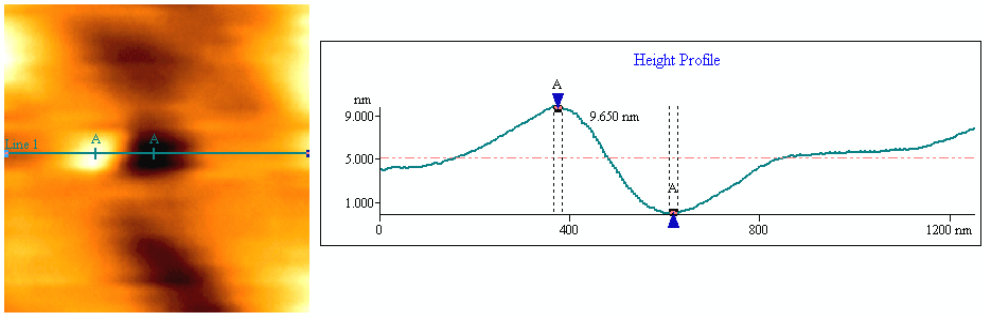

Figure 2. a) AFM image of a TEM Ni thin foil used in the experiments in which a nanoindentation near the edge of the inner hole can be observed (indicated by the arrow); b) shows a magnified image of the indentation with the corresponding topographic profile on the right.

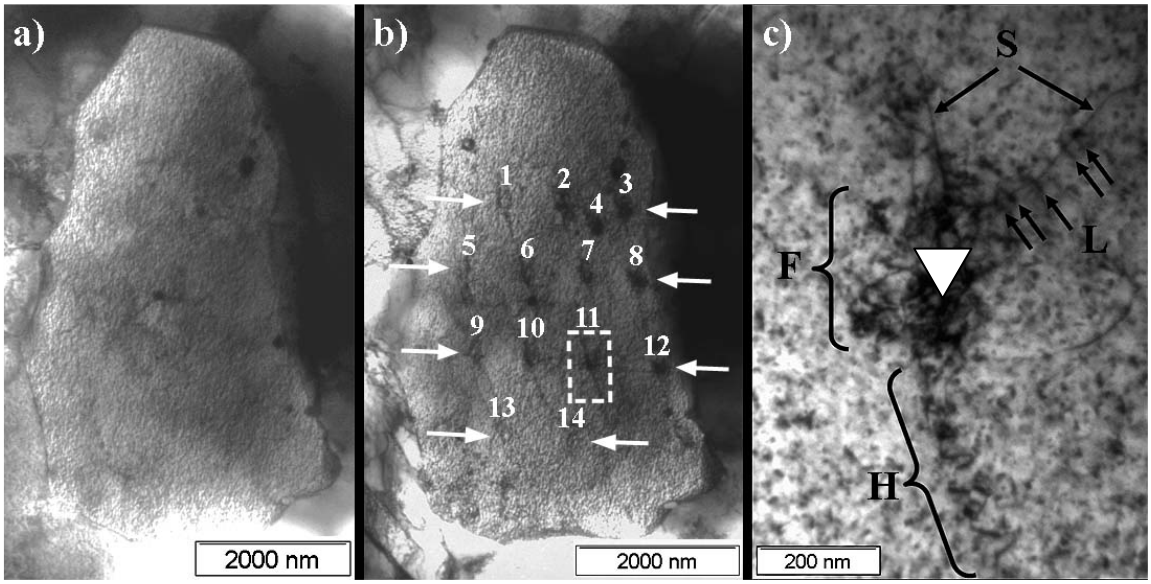

Figure 3. BF TEM images showing a dendrite in Ni before (a) and after (b) indentation testing with the DNISP probe. The white arrows in b) point to the direction of nanoindentation rows. c) Magnified detail of the indented region (delimited by a dashed rectangle in b)), evidencing a high dislocation density zone (F), straight dislocations (S), as well as helical/loop dislocations (H/L) piled up along three distinct crystallographic directions. The white triangle in c) marks the approximate contact region of the indenter with the sample.

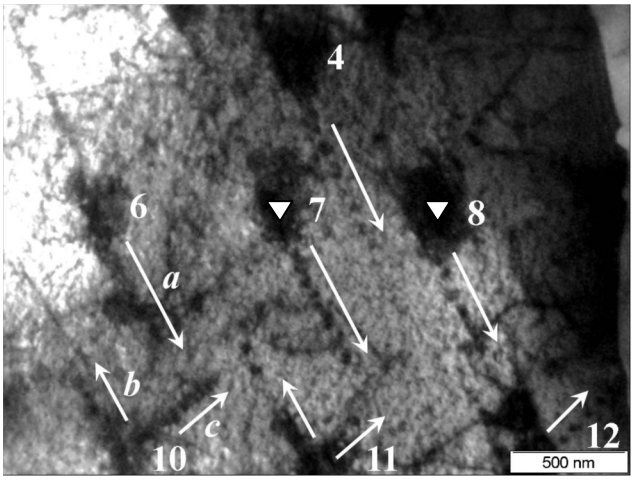

(a)

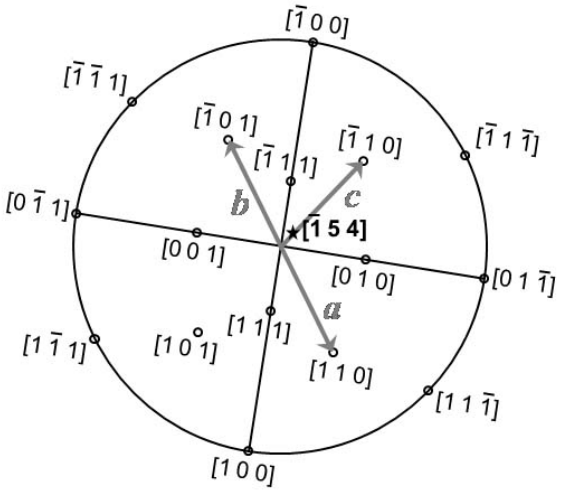

(b)

Figure 4. BF TEM image of indented regions (numbered) in the dendrite of Figure 1.b, taken with the electron beam approximately parallel to the direction. White arrows represent the gliding/pile up directions of loops and helices emitted from the centre of the indented regions; white triangles represent the projected area of the indenter in contact with the surface. b) Standard stereographic projection rotated to match the orientation of the SAD pattern obtained at the dendrite. The direction of load application is marked with a star.

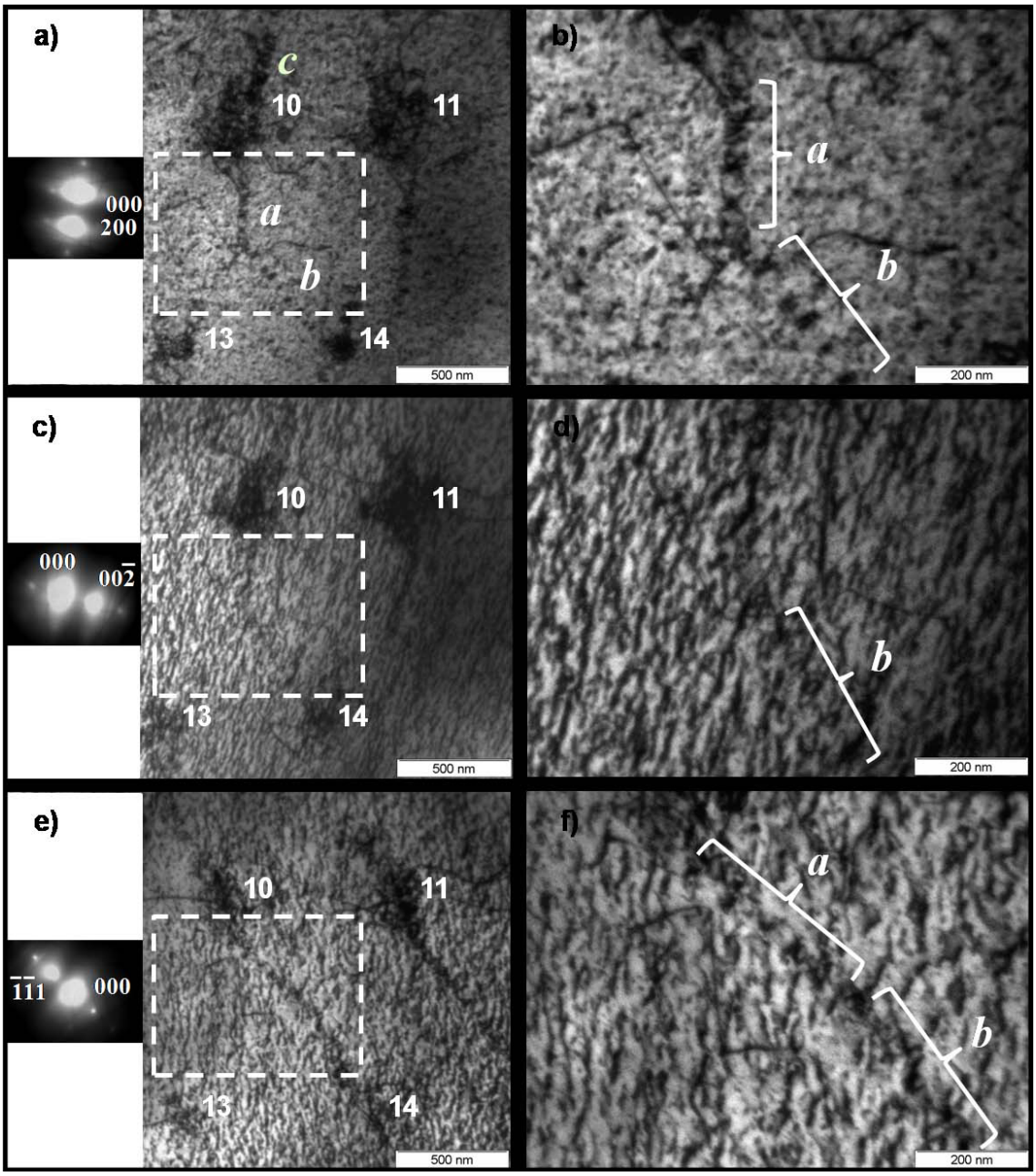

Figure 5. BF TEM images of indented regions (numbered) in the dendrite of Figure .b, taken under three different two-beam conditions: g = 200 (a) with a magnified detail in (b); g = $00\bar{2}$ (c) with a magnified detail in (d); g = $\bar{1}\,\bar{1}\,1$ (e) with a magnified detail in (f). In the left side of a), c) and e), SAD patterns corresponding to the different two-beam conditions are shown.

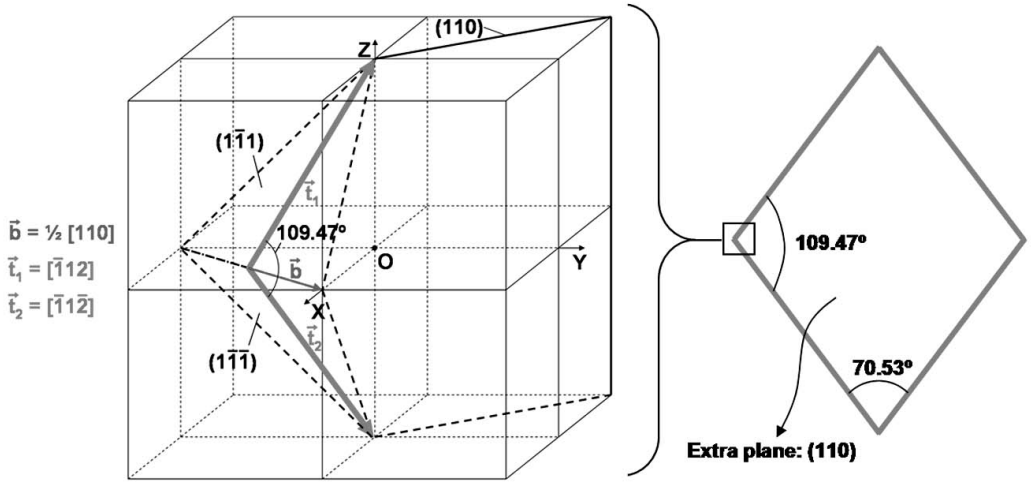

Figure 6. Schematic of two dislocation line segments of a dislocation loop, where vectors t_1 and t_2 represent their crystallographic direction (left); prismatic dislocation loop with the shape of a rhombus, formed by two linearly independent segments (right). Note that the two {111} planes on the right (not shown in the cube) are parallel to the ones on the left.

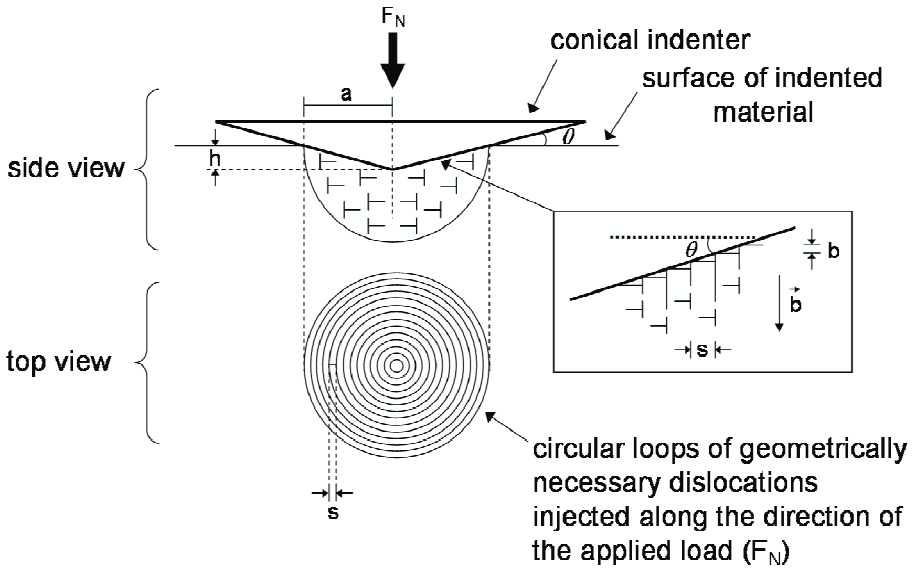

Figure7. Schematic representing the emission of geometrically necessary dislocation loops during the indentation of a single crystal with a conical indenter, as proposed by Nix and Gao [15].